(10) Neuenschwander, P. (Technisch-Chemisches Laboratorium, ETH Zentrum, CH-8092 Zurich), private communication, 1982.
(11) Charlet, G.; Delmas, G. *J. Macromol. Sci., Phys.*, submitted for publication.
(12) Charlet, G. Ph.D. Thesis, McGill University, Montreal, Canada, 1983.
(13) (a) Tani, S.; Hamada, F.; Nakajima, A. *Polym. J.* **1973**, *5* (1), 86. (b) Hoffman, A. S.; Frier, B. A.; Condit, P. C. *J. Polym. Sci., Part C* **1963**, *4*, 109.
(14) Filiatrault, D.; Delmas, G. *J. Polym. Sci., Polym. Phys. Ed.* **1981**, *19*, 689, 773.
(15) Phuong-Nguyen, H.; Delmas, G. *Macromolecules*, submitted for publication.
(16) Aharoni, S. M.; Charlet, G.; Delmas, G. *Macromolecules* **1981**, *14*, 1390.
(17) Dong, D. H.; Delmas, G., to be submitted for publication.
(18) Blais, P.; Manley, R. St. J. *J. Polym. Sci., Polym. Chem. Ed.* **1968**, *6*, 291.
(19) Keller, A.; Willmouth, F. M. *Makromol. Chem.* **1969**, *121*, 42.
(20) Wunderlich, B. "Macromolecular Physics"; Academic Press: New York, 1976; Vol. 2.
(21) Charlet, G.; Delmas, G. *Polym. Bull.* **1982**, *6*, 367.
(22) (a) Charlet, G.; Delmas, G.; Revol, J. F.; Manley, R. St. J. *Polymer* **1983**, *24*, 0000. (b) Charlet, G.; Delmas, G. *Ibid.* **1983**, *24*, 0000.
(23) Stofer, H.; Elias, H. G. *Makromol. Chem.* **1972**, *157*, 245.
(24) (a) Luisi, P. L.; Pino, P. *J. Phys. Chem.* **1968**, *72*, 2400. (b) Pino, P.; Luisi, P. L. *J. Chim. Phys.* **1968**, *65*, 130. (c) Pino, P.; Neuenschwander, P. *J. Polym. Sci., Polym. Symp.* **1975**, *51*, 171.
(25) Carlini, E.; Ciardelli, F.; Lardicci, L.; Menicagli, R. *Makromol. Chem.* **1974**, *174*, 27.

Microstructure in Linear Condensation Block Copolymers: A Modeling Approach

Michael A. Vallance† and Stuart L. Cooper*

Department of Chemical Engineering, University of Wisconsin, Madison, Wisconsin 53706.
Received August 15, 1983

ABSTRACT: X-ray scattering, differential scanning calorimetry, and dielectric spectroscopy have been combined to model the microstructure in linear thermoplastic condensation block copolymers where one block is semicrystalline. The materials characterized were segmented polyether–esters which exhibit properties between those of elastomers and tough plastics. Quantitative analysis of experimental data was used to evaluate a set of explicit modeling assumptions, regarding the nature of the crystalline and amorphous phases as well as the nature of the interdomain boundaries. The data generally supported the modeling assumptions of sharp interfaces between phase domains, minimal disorder in the polyester crystallites, nearly complete mixing of the chemically dissimilar sequences in the amorphous domains, predominantly three-dimensional (rather than one-dimensional) organization of the crystal–amorphous superstructure, and decreased self-diffusion among the amorphous sequences immediately adjacent to the (001) surfaces of the polyester crystallites. Microstructural parameters such as phase composition, crystallite size, and intercrystallite distance statistics were determined from the modeling studies. Subaudio frequency dielectric spectroscopy appears to be a useful technique for investigating interdomain boundary zone properties. Certain questions remain unresolved, such as to what extent is the crystalline phase continuous.

Introduction

Where polymer microstructures are heterogeneous, particularly when distinct phases coexist, the relationships between intrinsic phase properties and macroscopic properties are dictated by the spatial arrangement of phase boundaries and the properties of these boundaries. This is certainly true for thermomechanical, electrical, optical, and transport properties. These relationships can be used to quantify the design and selection of block copolymers, blends, interpenetrating networks, and polymer–filler composites for specific applications. Difficulty in evaluating the germane structural parameters tends to limit the usefulness of this approach to material design.

For linear condensation block copolymers, where the blocks are typically short and polydisperse, measurement of the various microstructural attributes is particularly difficult. Phase domains whose typical dimensions are a few nanometers tend to be difficult to resolve by microscopy. Although density and diffraction contrast mechanisms exist in principle, the small sizes are beyond the resolution of conventional transmission electron microscopy. Phase contrast microscopy can be used although the images can easily be misinterpreted.[1] The inability to prepare suitably thin representative (of bulk morphologies) films is a practical barrier.[2] Nor are the intrinsic properties of phases and interfaces easily accessible. Relevant investigations must identify both phase compositions and properties. Interdomain boundary zones of finite thickness can be distinguishable from the domain interiors in terms of both chemical composition and constraints on molecular mobility, although the second of these need not imply the first.

Among this class of materials are the linear block copolymers formed with alternating segments of poly(tetramethylene terephthalate) (PTMT) and poly(tetramethylene oxide) (PTMO). The PTMT segments are capable of partial crystallization. In most published studies[3-6] the PTMO segments are derived from approximately 1000 molecular weight polydisperse α-hydro-ω-hydroxypoly(tetramethylene oxide) oligomers. PTMO crystallization appears to be suppressed during solidification of the undiluted polymer melts.

Differential scanning calorimetry (DSC) studies[5] of these segmented polyether–esters confirm that an amorphous phase of mixed chemistry coexists with a PTMT crystalline phase in samples prepared from undiluted melts. Broad thermal glass transitions and aging effects[7] suggest that the amorphous regions are not without some heterogeneous structure. Lilaonitkul et al. have shown that the thermal glass transition midpoints of the PTMO–PTMT systems

† Present address: Chemical Laboratories, General Electric Corporate Research and Development, Schenectady, NY 12345.

0024-9297/84/2217-1208$01.50/0

Table I
Stoichiometric and Calorimetric Data

polymer	$A/B/C$[a]	u_2[b]	w_2[c]	T_h,[d] K
H1	3.6/2.6/1	0.465	0.113	478
H2	5.9/4.9/1	0.588	0.226	486
H3	7.5/6.5/1	0.645	0.284	487
H4	9.8/8.8/1	0.703	0.330	489
H5	17.3/16.3/1	0.807	0.403	492
H6	28.0/27.0/1	0.871	0.423	493
H7	1.0/1.0/1	1.000	0.475	495

[a] A, B, and C are the mole ratios of dimethyl terephthalate, 1,4-butanediol, and α-hydro-ω-hydroxypoly(tetramethylene oxide). [b] u_2 is the overall polyester weight fraction. [c] w_2 is the polyester crystalline weight fraction from integrated melting enthalpy in 10 K/min DSC traces. [d] T_h is the highest observed melting temperature from 10 K/min DSC traces.

follow the averaging rule proposed by Gordon and Taylor[8] for random copolymers.

Lilaonitkul et al.[5] used light scattering to point to the existence of several distinctive spherulitic textures in PTMO–PTMT block copolymers, relating to the orientation of crystallized polyester chains with respect to the radial direction in the spherulites. Whereas solution-cast films tended to have chains perpendicular to the radial direction, melt-cast films produced structures where the PTMT chains angled approximately 45° from the radial direction. Matsuo et al.[9] have identified these same structures; they note that the scattering patterns from the latter structure identify it as a two-dimensional axialite rather than a three-dimensional spherulite.

Dynamic mechanical temperature scans[4,5,10] show these copolymers to be thermoplastic elastomers. Strain hardening is accompanied by permanent set at all but the smallest strains.[5]

Small-angle X-ray scattering (SAXS) from quenched PTMO–PTMT films was found to be consistent with a model of stacked lamellae of alternating phase, after the isotropic scattering pattern had been Lorentz corrected and Fourier transformed into a one-dimensional correlation distance space.[11] In that same study an interlamellar transition zone of varying electron density was estimated to be 0.9-nm thick, independent of the number-average PTMT sequence degree of polymerization $\langle x \rangle$.

In this study an attempt has been made to use several different techniques to examine different aspects of microstructure in segmented PTMO–PTMT copolymers. The experiments include DSC and SAXS as well as X-ray diffraction at higher angles and dielectric spectroscopy. In order to provide useful quantitative microstructural parameters, the measured data are compared to predictions based on a three-dimensional model of microstructure. Although the model is somewhat speculative, it can be judged on its ability to explain a variety of physical measurements and observations in a rational fashion.

Experimental Section

Materials. The block copolymers studied were formed by melt transesterification of 1,4-butanediol, dimethyl terephthalate, and polydisperse α-hydro-ω-hydroxypoly(tetramethylene oxide) with a number-average molecular weight of 1000.

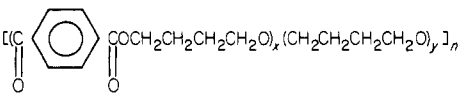

Here y averages 12–13. The number-average molecular weight of the copolymers is typically 25 000–30 000. The value of x can be related to the molar ratios in the reaction mixture. A series of six well-characterized segmented polyether–esters were supplied by E. I. du Pont de Nemours and Co. These are listed in Table I as H1 through H6, along with calorimetric data. H7 is the related polyester homopolymer, supplied by the Tennessee Eastman Co.

Sample Preparation. Samples were filtered prior to molding and then precipitated from 1,1,2-trichloroethane at 297 K, using methanol as the nonsolvent. This procedure was used only for H1–H6, not for H7. After decanting and drying in vacuum at 398 K, the precipitates were molded into disks by compression molding in a hydraulic press with platen heaters. After heating the polymers to temperatures 25 K above their as-received DSC melting endotherms, a pressure of 1000 N/cm^2 (gauge) was applied. Temperature and pressure were held constant for 10 min before the pressure was released and the mold was quenched in ice back to room temperature. Sample thickness was varied by varying the thickness of the mold cavity from 0.01 to 0.2 cm. Samples were stored at 297 K in vacuum prior to use.

Experimental Procedures. DSC traces were recorded for 0.015–0.02-g samples cut from compression molded films. Aluminum pans were used both to hold the sample and as the reference. Traces were measured under flowing helium at 5, 10, and 20 K/min scanning rates on a Perkin-Elmer DSC-2C instrument. At each rate, the temperature scale was calibrated by using mercury and indium melting as reference points. These data were used to measure the PTMT melting enthalpies and temperatures which are presented in Table I.

Density measurements were made at 297 K on melt-cast samples of approximately 10-g mass. Sample weights measured in air and upon immersion in Dow Corning 200 fluid, a dimethylpolysiloxane of known density, were used to calculate sample densities which are summarized in Table II.

X-ray scattering powder patterns for crystallographic analysis were obtained in symmetric reflection at room temperature for 0.02-cm-thick melt-cast films. The Picker instrument was operated at 35 kV and 15 mA. The copper anode was adjusted for a 4.5° take-off angle in the horizontal plane, and the resultant beam had a Gaussian profile with a width at half-height of 0.1° with respect to the anode-to-sample distance. The matched divergence and receiving slits provided for 1° divergence. The scattering slit width was chosen wide enough to measure parafocused scattering from all depths. In the vertical direction beam divergence was minimized by stacks of Soller slits in the paths of the incident and scattered beams. A nickel foil reduced the contribution of Cu Kβ radiation. Signals from the scintillation counter were conditioned by a discriminating pulse height analyzer. The time constant of the signal averaging circuit was 10 s and the angular speed of the rotary table was 0.125°/min in

Table II
Dilatometry and Crystallography Data

polymer	ρ,[a] g/cm^3	v_2[b]	ρ_1,[c] g/cm^3	D_{100},[d] nm	D_{010},[e] nm	w_2[f]
H1	1.088	0.088	1.058	6.0	6.8	0.101
H2	1.155	0.186	1.098	9.0	10.5	0.205
H3	1.182	0.239	1.112			
H4	1.208	0.284	1.131	9.1	10.8	0.315
H5	1.249	0.359	1.162			
H6	1.272	0.384	1.190	10.5	12.2	0.412
H7	1.311	0.444	1.238	14.3	15.0	

[a] ρ is the measured density. [b] v_2 is the crystalline volume fraction. [c] ρ_1 is the amorphous-phase density. [d] D_{100} is the average crystal thickness in the [100] lattice direction. [e] D_{010} is the average crystal thickness in the [010] lattice direction. [f] w_2 is the overall polyester crystalline weight fraction from the fraction of intensity diffracted into crystalline reflections.

terms of scattering angle. Measurements were made in the scattering angle (2θ) range 5–35° after it was determined that no diffraction lines were apparent at higher angles. Powder profiles were digitized and then corrected for dark current, parasitic scattering, sample transmittance and thickness, and polarization.[12]

Isotropic SAXS patterns were recorded in transmission from 0.05-cm-thick compression-molded films at room temperature for scattering angles up to 11.5° at intervals of 0.0573°. The instrument used nickel-filtered Cu radiation from a rotating-anode generator operated at 40 kV and 160 mA. Four-slit Beeman-type collimation was employed using slits which were 1 by 0.025 cm. Slit pairs were spaced at 50 cm while the sample-to-detector distance was 75 cm. The collimation path and sample were enclosed and purged with helium at a slight pressure over atmospheric in order to minimize parasitic scattering. Intensity was measured at each angle for 200 s using a proportional counter in conjunction with a pulse-height discriminator whose window was centered about Cu Kα energy. Data collection and stepping motor control of the counter position were automated through a Digital Automation Model 300 data acquisition and control system. The data were corrected for dark current, parasitic scattering, sample transmittance and volume, main beam intensity, and polarization. Scattering patterns were desmeared to eliminate the effect of finite-height collimation using the iterative method of Lake.[13] The normalized and desmeared intensity from a calibrated Lupolen (polyethylene) standard was used to restate the intensities on an absolute basis.[14]

Dielectric measurements were done at 297 K on the frequency range 0.0001–20 Hz using a computer-interfaced, frequency-domain spectrometer.[15,16] Compression-molded disks were coated with metallic electrodes which were sublimated from tungsten baskets in a Hitachi HUS-5GB vacuum system. A guard-ring electrode was masked off around the measurement electrode in order to eliminate edge effects. In a range of thicknesses from 0.05 to 0.2 cm in conjunction with electrodes of gold, copper, and platinum, no differences could be detected in the various spectra. It was therefore concluded that any electrode polarizations were negligible, and no attempt has been made to correct for them. Water uptake proved to cause tremendous electrode polarizations;[15] all spectra shown here are for polymers dessicated for at least 100 h at 297 K in 10^{-8} N/cm^2 vacuum before application of the electrodes. Testing was carried out in vacuum where the films were supported in a Balsbough LD-3 research cell.

Analysis of Experimental Data

Modeling Approach. In the course of analyzing the experimental data, several assumptions have been made: (1) All segmented polyether–esters form two-phase morphologies. One phase consists of polyester crystallites, while the other is a mixture of amorphous polyether and polyester sequences. The compositional transition between phases is assumed to be relatively sharp. (2) Each crystalline domain is assumed to be a single crystal. These may or may not be interconnected. The crystals are similar in shape and size. (3) Flory melting point depression theory[17] is assumed applicable to the calculation of equilibrium melting at ambient pressure. (4) Transport properties in amorphous regions immediately adjacent to the crystallites may be altered due to constraints on chain mobility placed by the immobilized covalent bonds on the interfaces.

Differential Scanning Calorimetry. Figure 1 shows the DSC melting endotherms for 10 K/min heating scans of the six segmented polyether–esters. Scans at 5 and 20 K/min produced nearly identical traces, so that rate effects were minimal. In order to integrate the areas of the melting endotherms, it was necessary to construct baselines in the temperature range of the endotherms. Runt and Harrison[18] review a number of approximate methods that have been used to accomplish this. In the present case, three criteria have been used to construct these baseline curves: (1) The baseline curves have a constant, positive radius of curvature. (2) The curves are tangent to the actual traces at their intersections. (3) The curves overlay

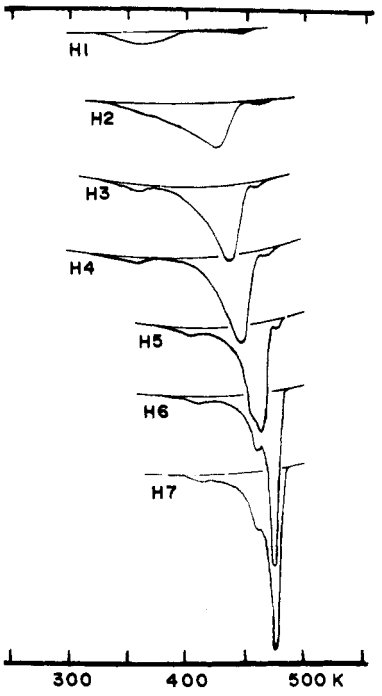

Figure 1. 10 K/min DSC heating scans of PTMT melting endotherms.

the actual traces for at least 5 K on both sides of the endotherms. While this procedure is not quantitatively rigorous, it does provide for nonarbitrary selection of baseline curves. Baselines so constructed are shown in Figure 1. The traces were digitized and the melting endotherm areas were integrated numerically and normalized for sample weight. To obtain absolute melting enthalpies, a scaling constant was used based on the area inside the indium melting endotherm and the melting enthalpy of indium, 28.4 J/g. The overall crystalline weight fraction w_2 in Table I was calculated directly from the melting enthalpy using the reported heat of fusion for the α form of the PTMT crystal, 144.5 J/g.[19] As expected, w_2 increases monotonically with the overall PTMT weight fraction u_2 throughout the range of materials tested. As noted by Lilaonitkul et al.,[5] the fraction of the total PTMT mass that crystallizes is on the order of 0.5 or less. In Figure 1 it is seen that several of the copolymers exhibit two or three overlapped endothermic maxima during heating through the melting range. The subsidiary maxima are tentatively assigned to melting of relatively short crystalline stems.

The same analysis was used to determine the highest temperature T_h at which melting was observed. Within 1 K this value was the same at all heating rates. The values for 10 K/min traces are reported in Table I. To compare this value to the equilibrium melting point T_m, a series of isothermal crystallizations were done in the DSC at different temperatures T_c in the case of polymer H2. During subsequent heating scans, the temperature T_p at which the power input was maximum was recorded. Following Hoffman and Weeks[20] a plot of T_c vs. T_p was linearly extrapolated to the point where the two were equal. The actual intersection should be T_m. The Hoffman–Weeks analysis relies on extrapolation from a temperature range where it is possible to nucleate crystallization into a range where it is not. This procedure contributes a great deal of uncertainty in the case of short-segment block copolymers due to the large amount of subcooling necessary to nucleate crystallization. In the case of H2, it was necessary to hold the temperature at 450 K or lower in order to crystallize a detectable mass inside of 20 min. This

resulted in an extrapolation over a 39 K range and little confidence can be placed in the result of 489 K. It does compare qualitatively with the value of T_h = 486 K from Table I.

The equilibrium melting point T_m can be predicted with a model based on the melting point depression theory proposed by Flory.[17] The main assumptions are as follows:

1. The distribution of degrees of polymerization for the crystallizable blocks is approximately geometrical; i.e., the fraction of crystallizable blocks with degree of polymerization x is $(1-p)p^{x-1}$, where x is a positive integer and p is a constant in the range 0–1. No assumptions need be made regarding the distribution of lengths for the blocks of the noncrystallizable component.

2. At $T = T_m$, two homogeneous phases exist, a randomly mixed liquid of both components and a perfectly ordered crystalline phase of the crystallizable component only. The liquid phase is compatible with the liquid lattice description, where the two components coexist on the same statistical lattice. Enthalpy in the liquid phase is described approximately by a van Laar expression. Configurational entropy calculations for the liquid phase are limited to consideration of the liquid lattice assignments. Entropy from other sources is ignored.

A simplifying assumption is to neglect the effect of chain ends, because their concentration is very low compared to the concentration of interblock junction points. The resulting expression is

$$1/T_m - 1/T_{m0} = -(R/h_u)[\chi(1-v_a)^2 + \ln p] \quad (1)$$

where T_{m0} is the melting point of the homopolymer of the crystallizable component, R is the gas constant, h_u is the molar heat of fusion of the crystallizable component, χ is the Flory interaction parameter for the two components, and v_a is the fraction of equivalent lattice sites, i.e., the volume fraction, occupied by the crystallizable component at $T = T_m$ in the absence of any crystallinity.

Of the two terms in brackets in eq 1, the first is related to the enthalpy of mixing the two components in the liquid phase. The interaction parameter is positive for positive heats of mixing. For such cases the effect would be to elevate T_m relative to T_{m0}, according to eq 1. For χ much different from zero, the assumptions of random placement on the liquid lattice and nonspecific interchain interactions only are questionable. Where χ is temperature or concentration dependent, then the value of χ in eq 1 is for vanishing crystalline fraction and $T = T_m$.

The second bracketed term is related to the entropy of forming crystals of uniform thickness pure in the crystallizable component from the available finite-length sequences. The effect of decreasing the degree of polymerization of the sequences of the crystallizable component is to depress T_m relative to T_{m0}.

From Table I it can be seen that T_h decreases with decreasing p (and decreasing $\langle x \rangle$, the number-average degree of polymerization for the PTMT sequences), so that the entropy term dominates in eq 1. In light of this observation and the general trend of χ to decrease with increasing temperature, it was not surprising that eq 1 gave quantitative predictions of T_m with $\chi = 0$ and T_h approximating T_m. The data are compared to eq 1 in Figure 2 with $\chi = 0$, T_{m0} = 495 K, and h_u = 31.8 kJ/mol.[19]

Wide-Angle X-ray Scattering. Wide-angle X-ray scattering measurements exhibited nine diffraction maxima in the scattering angle range 5–35°. The diffraction patterns are shown for five of the polymers including H7, the polyester homopolymer, in Figure 3. These patterns are corrected for air scattering, dark current, sample transmittance and thickness, and polarization of the

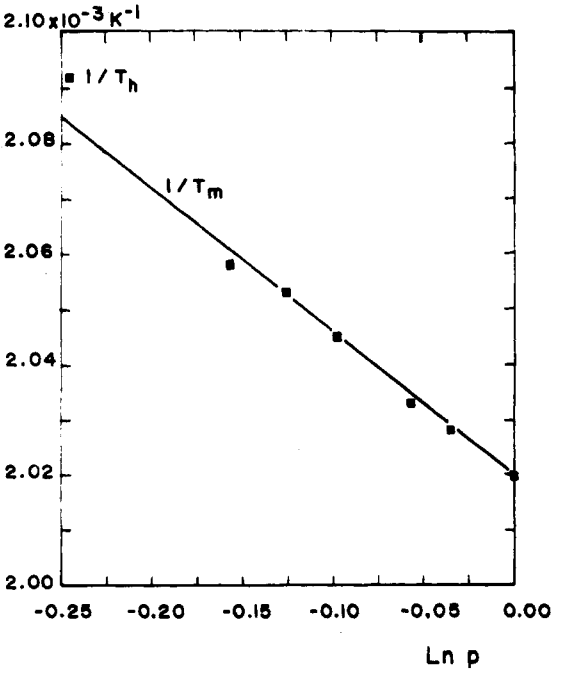

Figure 2. Comparison of melting point data with melting point depression theory.[17]

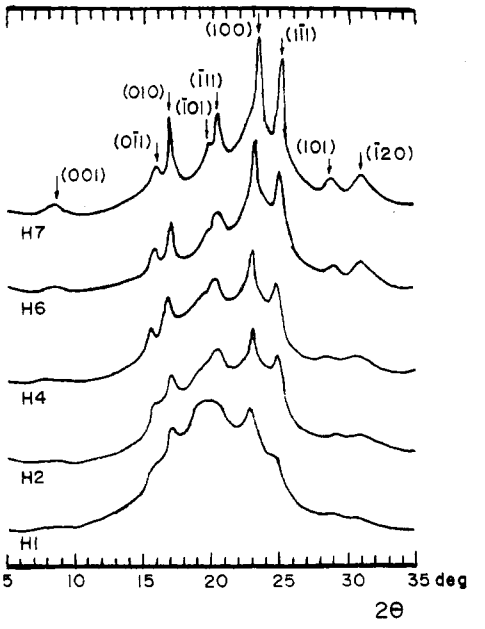

Figure 3. Corrected isotropic X-ray scattering patterns.

scattered radiation. The data were used for determination of the unit cell in the polyester crystals, the density of those crystals, the size of the crystals, and the degree of crystallinity.

Several researchers have studied the diffraction patterns of PTMT,[21,22] and there is general agreement that two distinct unit cells exist. Whereas isotropic films quenched from the molten state exhibit the α phase, under moderate uniaxial strains these same films are seen to exhibit both α and β phases, while at elongations on the order of 12% only the β phase is present. The β phase exhibits more extension in the axial direction, having a repeat distance of 1.295 vs. 1.159 nm for the α phase. The difference arises primarily in the conformation of the tetramethylene sequence. The locations of the Bragg angles for nine lattice planes in the α phase unit cell proposed by Tadokoro et al.[21] are displayed over the H7 diffraction pattern in Figure 3. The unit cell is triclinic with one polymer repeat unit

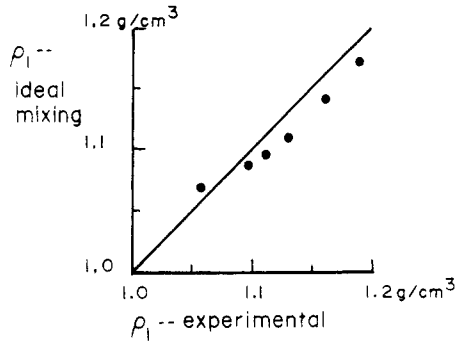

Figure 4. Comparison of amorphous-phase density calculations from measured density vs. ideal mixing model.

(two polyester linkages) per cell. The cell parameters are $a_1 = 0.483$ nm, $a_2 = 0.594$ nm, and $a_3 = 1.159$ nm, with $\alpha_1 = 99.7°$, $\alpha_2 = 115.2°$, and $\alpha_3 = 110.8°$. The calculated density of this cell is 1.403 g/cm^3. As seen from Figure 3 this unit cell accurately predicts the angular positions of all nine diffraction maxima.

Assuming two phase microstructure with sharp interfaces, the macroscopic density values in Table II can be used with the calculated crystalline weight fractions and the crystalline density to calculate both the amorphous-phase density and the crystalline-phase volume fraction:

$$v_2 = w_2(\rho/\rho_2) \tag{2}$$

$$\rho_1 = (\rho - v_2\rho_2)/(1 - v_2) \tag{3}$$

where v_2 is the crystalline-phase volume fraction, w_2 is the crystalline-phase mass fraction, ρ is the macroscopic density, ρ_2 is the crystalline-phase density, and ρ_1 is the amorphous-phase density. The calculated values of v_2 and ρ_1 have been listed in Table II. It has been assumed in these calculations that the crystalline phase exhibits minimal paracrystalline disorder[23] of the second kind such as dislocations and strains and of the first kind such as substitutions, interstitials, and vacancies. No assumption has been made about the nature of volumetric mixing in the amorphous phase. The density of that phase is seen to increase monotonically with u_2, the overall polyester mass fraction. The amorphous phase density of H7 is calculated as 1.238 g/cm^3, which should correspond quite closely to the density of amorphous PTMT, while the density of the subcooled 1000 molecular weight α-hydro-ω-hydroxy polyether oligomeric liquid at 298 K is 0.98 g/cm^3. Increasing the concentration of PTMT in the amorphous phase tends to increase the density of that phase. A mixture rule based on additivity of specific volumes is approximately applicable as shown in Figure 4:

$$1/\rho_1 = w_t/\rho_t + w_0/\rho_0 \tag{4}$$

where w_t is the mass fraction of PTMT in the amorphous phase $[(u_2 - w_2)/(1 - w_2)]$, ρ_t is the density of amorphous PTMT ($\sim$1.238 g/cm^3), w_0 is the mass fraction of PTMO in the amorphous phase $[(1 - u_2)/(1 - w_2)]$, and ρ_0 is the density of amorphous PTMO ($\sim$0.98 g/cm^3).

The corrected scattering patterns in Figure 3 can be divided into diffraction lines and diffuse scattering. Broadening of the diffraction lines arises due to several factors:[24] optical and electronic broadening, broadening due to paracrystalline disorder of the second kind, and small crystal size. Whereas rigorous deconvolution of the instrumental effects is possible in theory, satisfactory corrections are conventionally made by comparing the broadening with that in patterns from powders of relatively large and perfect crystals. These powders must be prepared into films of the same thickness as the samples and the crystals must be chosen so as to give readily apparent diffraction lines in the same range of scattering angle where the diffraction lines of the samples occur. For this purpose a powder of high-carbon, low-silicon steel was used as the standard. The metastable iron carbide (cementite) orthorhombic phase was present in high concentration, and exhibited six diffraction lines between 19 and 27° of scattering angle. The powder, whose particles were on the order of 5–10 μm in size, was adhered to a glass slide with an amorphous binder so as to form a patchy 0.02-cm coating. The diffraction lines were extremely narrow and it was assumed that in this case broadening was due to instrumental factors only. The shape of the diffraction line profiles in the sample films and the standard were well approximated by Cauchy functions, so that integral breadths β free from broadening artifacts could be calculated from integral sample breadths β_1 and interpolated integral standard breadths β_2.[24]

$$\beta = \beta_1 - \beta_2 \tag{5}$$

where the integral breadth is calculated as

$$\beta_i = \int I(2\theta)\ \mathrm{d}(2\theta)/I(2\theta_{hkl}) \tag{6}$$

Here $I(2\theta)$ is the measured intensity, and $I(2\theta_{hkl})$ is the measured intensity at the Bragg scattering angle for the spacing between (hkl) lattice planes. This definition of integral breadth is appropriate for calculating either β_1 or β_2. The range of integration should contain all perceptible diffracted intensity associated with the particular line. Where lines tend to overlap, it is better to fit the apparent shape with a Cauchy function and use the two parameters of the fit to calculate the integral breadth; this approach was used here. The corrected breadths were used with the Scherrer equation:

$$D_{hkl} = \lambda/(\beta \cos \theta_{hkl}) \tag{7}$$

where D_{hkl} is the mean crystal thickness in the $[hkl]$ lattice direction and λ is the wavelength of the monochromatic primary beam (0.1542 nm). No attempt was made to separate out broadening due to lattice distortions, because no second-order reflections were present.[24] For that reason, the calculated crystal sizes should be regarded as lower limits. The analysis was done only for the [100] and [010] directions which form angles of 99.7 and 115.2°, respectively, with the [001] direction and 110.8° with each other. The (001) reflection was in all cases very broad, suggesting that D_{001} is very small, on the order of a few nanometers. Due to the small intensity associated with (001) diffraction, no attempt has been made to calculate D_{001}. Values for D_{100} and D_{010} are listed in Table II. The values tend to be quite uniform between samples and between the two directions, except for H1 where they are much smaller and H7 where they are somewhat larger.

Several authors have proposed techniques for the measurement of the crystalline weight fraction using diffraction powder patterns. The method used here was proposed by Ruland.[25] The technique has been modified for use with the present set of data where the chemical composition of the crystalline and amorphous regions is different and where the overall chemical composition varies from sample to sample. Rather than calculating the generalized dislocation factor $D^2(q)$ in the iterative fashion proposed by Ruland, the crystalline weight fraction of H7 has been assumed equal to that estimated from the heat of fusion (Table I), in order to provide a calibration point. Equation 8 has been used to calculate the crystalline weight fractions

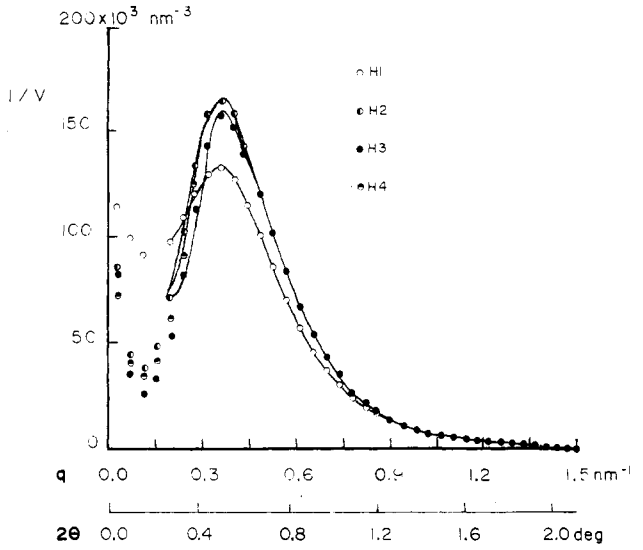

Figure 5. Corrected isotropic X-ray scattering patterns. Curves are best fits of kinematic SAXS model.

in Table II, where a k value of 0.93 has been used on the basis of analysis of the data for sample H7:

$$w_2 = \left[\left(\int q^2\langle f_i^2\rangle \, dq\right)\left(\int q^2 I_d \, dq\right) \times (\Sigma\phi_{2i}m_i)\right] \Big/ \left[k\left(\int q^2\langle f_i^2\rangle_2 \, dq\right)\left(\int q^2 I \, dq\right)(\Sigma\phi_i m_i)\right] \quad (8)$$

where $q = (4\pi/\lambda)\sin\theta$, $\langle f_i^2\rangle = \sum\phi_i f_i^2(q)$, ϕ_i is the number fraction of atom i in the polymer, $f_i(q)$ is the atomic form amplitude of atom i, $I_d(q)$ is the portion of isotropic scattering intensity appearing in the crystalline diffraction lines, ϕ_{2i} is the number fraction of atom i in the crystalline phase, m_i is the mass of atom i, $k = (\int q^2\langle f_i^2\rangle_2 D^2 \, dq)/(\int q^2\langle f_i^2\rangle_2 \, dq)$, $\langle f_i^2\rangle_2 = \sum\phi_{2i}f_i^2(q)$, $D^2(q)$ is the apparent generalized dislocation factor for the crystalline phase, and $I(q)$ is the total (diffracted plus diffusely scattered) isotropic scattering intensity. Inclusion of the factor D^2 accounts for first and second kind lattice distortions including random thermal vibrations, which cause a fraction of the intensity scattered by the crystalline volume to appear in the "amorphous halo" rather than in the crystalline lattice. $D^2(q)$ has been assumed constant between samples in this set; the crystallite size is assumed to change, but not crystallite perfection. Equation 8 is rigorous for nonoverlapping atoms when the integrations are done on the range 0–∞. In the present study the integrals of measured values have been calculated in the 2θ range 5–35°. Above 35°, little coherent scattering is observed, while the small-angle scattering at scattering angles 2θ below 5° contributes little to the integrals. The integrations involving form amplitudes were done over the same range. A low-level background, including Compton scattering, was subtracted prior to integration. Digitized tabulations of the measured intensity and readily available atomic form factor tables were used to numerically evaluate the integrals. The agreement between the calorimetry-derived w_2's in Table I and those from diffraction measurements in Table II are quite good, although it should be noted that the two sets of values are not derived in a totally independent fashion.

Small-Angle X-ray Scattering. Small-angle X-ray scattering patterns were obtained for H1, H2, H3, and H4. All four isotropic patterns are shown in Figure 5 as discrete data points; the solid lines are model fits as described below. The data have been corrected for dark current, parasitic scattering, finite beam height effect; and polarization. They have been normalized for differences in film transmittance, primary beam intensity, and illuminated volume. The low-angle tail of the diffuse wide-angle scattering component was approximately subtracted by fitting the scattered intensity to a two-parameter equation ($I_b(q) = k_1\exp(k_2q^2)$) in the 2θ range 2–6° and subtracting this function from the observed intensity. This approximate technique for eliminating intraphase scattering was justified, since no attempt has been made to specifically analyze the high-angle tail of the small-angle scattering, as is done in cross-boundary, transition-zone thickness calculations. By eliminating I_b, which amounted to less than 0.5% of the total intensity at the scattering maximum, the phases could be modeled as isotropic, homogeneous continua for the purpose of SAXS analysis.

As seen in Figure 5, the intensity profiles for H2, H3, and H4 are very similar, while that for H1 is somewhat broader and lower. In light of the different v_2 values among these polymers, the coincidence of the three scattering patterns suggests a counterbalancing variation in another morphological parameter. That parameter is ξ, the difference in electron density (electrons/nm³) between the crystalline and amorphous phases:

$$\xi = \rho_2\Sigma(\phi_{2i}z_i/m_i) - \rho_1\Sigma(\phi_{1i}z_i/m_i) \quad (9)$$

where z_i is the atomic number of atom i and ϕ_{1i} is the number fraction of atom i in the amorphous phase. Equation 9 has been used with previously tabulated values of ρ_1 and w_2 to calculate the values of Table III, denoted as ξ'. They are seen to systematically decrease as the concentration of polyester in the amorphous phase increases.

To gain further insights from the SAXS patterns, a kinematic scattering model has been used. Polyester crystallites are approximated as ellipses of revolution, in which it is envisioned that the [001] direction of the crystallite approximately coincides with the axis of symmetry of the ellipsoid. Diffraction line broadening analysis showed the crystallites to have similar average dimensions in the [100] and [010] lattice directions, suggesting the symmetry. At first glance, this model seems incongruous with the lamellar architecture which other researchers have proposed for these polymers. However, a set of oblate spheroids, if positioned edge to edge, would result in a scattering profile very similar to what might be expected from stacks of lamellae. Whereas lamellar stacks are basically one-dimensional in nature, the ellipsoidal particles proposed here serve as the basic unit of a rational three-dimensional structure.

Quenched films, 10–20 μm in thickness, prepared for this study did not show resolvable, classical spherulitic texture in a polarized-light microscope (Unitron U11) at magnifications up to 2000×. The films, however, were highly structured and birefringent, suggesting that the polymer morphologies are made up of regions, 0.2 μm or larger in dimension, characterized by optical anisotropy, and, therefore, by preferred orientation of polyester and/or polyether sequences. The minimum number of crystallites in such a region can be estimated by using Bragg's law[24] with the value of θ where the SAXS maximum occurs to estimate the average volume associated with one crystallite and comparing this to the minimum volume of the superstructure. The result is about 500 crystallites per superstructure. Similar orientation, with respect to lattice directions, among the set of crystallites in a given superstructure would explain the observed optical anisotropy. This orientation might arise during melt casting due to the movement of a planar solidification front through a region; it is expected that the crystals would have a preferred orientation with respect to such a front.

Table III
Small-Angle X-ray Scattering

polymer	ξ',[a] nm^{-3}	ξ,[b] nm^{-3}	$\langle l_3 \rangle$,[c] nm	$\langle l_1 \rangle$,[d] nm	$\langle A_1 \rangle$,[e] nm	$\langle A_3 \rangle$,[f] nm	δ_s,[g] nm
H1	99	102	2.7	6.0	15.0	10.9	4.6
H2	87	85	2.3	10.0	15.2	12.0	3.3
H3	83	78	2.8	9.9	14.9	11.3	3.0
H4	78	74	3.1	9.7	14.5	11.2	3.0

[a] ξ' is the electron density difference between phases from phase compositions and mass densities. [b] ξ is the electron density difference between phases from model fit to SAXS data. [c] $\langle l_3 \rangle$ is the average crystal thickness in the [001] direction of the superlattice. [d] $\langle l_1 \rangle$ is the average crystal thickness in the directions perpendicular to the [001] direction. [e] $\langle A_1 \rangle$ is the average intercrystallite distance in the [100] and [010] directions of the superlattice. [f] $\langle A_3 \rangle$ is the average intercrystallite distance in the [001] direction of the superlattice. [g] δ_s is the scalar fluctuation width, a measure of paracrystalline disorder of the second kind in the superlattice.

Along a given chain a broad distribution of crystallizable polyester sequence lengths interspersed with variable lengths of polyether could exhibit tight folds only with the longer polyester sequences. Polyester sequences separated by one or more polyether sequences could easily crystallize into neighboring crystallites with the connecting polymer chain contributing to the transcrystalline amorphous network. Sizable numbers of amorphous sequences connecting the (001) face of one crystallite with that of another would wield considerable force in maintaining orientation and relative position between neighboring crystallites. The positional organization of the crystallites has been approximated by locating them on a three-dimensional paracrystalline lattice. In the present case, the crystallites are located at the lattice points of a simple tetragonal paracrystalline superlattice, where the [001] direction in the polyester crystallites is aligned with the [001] direction in the paracrystalline superlattice. This approach acknowledges the possibility of differing periodicities in the chain axis and transverse directions. Superstructure size effects are neglected because even a small effective superstructure ($\sim$0.2 μm) would contain many lattice points. The entropic forces responsible for short-range order in the superlattice have no long-range corollary. It is therefore sufficient to include only lattice distortions of the second kind,[23] and for computational efficiency these are assumed to be Gaussian and isotropic.

$$I(q)/V = (1/v_s)\langle f_s^2(\mathbf{q}) Z_s(\mathbf{q}) \rangle_q \qquad (10)$$

where $I(q)$ is the isotropic scattering intensity function, V is the scattering volume, and v_s is the average volume associated with an individual superlattice point.

$$f_s(\mathbf{q}) = (4\pi cR^3\xi/3)(3/\zeta^3)(\sin\zeta - \zeta\cos\zeta)$$

where cR is the half-length of an ellipsoid along its axis of symmetry and R is the radius of an ellipsoid.

$$\zeta = Rq(c^2\cos^2\phi + \sin^2\phi)^{1/2}$$

where ϕ is the angle subtended by $\mathbf{q}$ and the axis of symmetry of an ellipsoid.

$$\mathbf{q} = (2\pi/\lambda)(\mathbf{s} - \mathbf{s}_0)$$

where $\mathbf{s}$ is the unit vector in the scattering direction of interest and $\mathbf{s}_0$ is the unit vector in the direction of the primary beam.

$$Z_s(\mathbf{q}) = \prod_{k=1}^{3} \mathrm{Re}\{[1 + F_k(\mathbf{q})]/[1 - F_k(\mathbf{q})]\} \qquad (\mathbf{q} \neq \mathbf{0})$$

and

$$F_k(\mathbf{q}) = \exp(-\delta_s^2 q^2/2)\exp(-i\mathbf{q}\cdot\langle \mathbf{A}_k \rangle)$$

where δ_s is the scalar fluctuation width, $\langle \mathbf{A}_k \rangle$ is the kth (k = 1, 2, or 3) average paracrystalline lattice vector, and $\langle\rangle_q$ indicates an average over all $|\mathbf{q}| = q$. The lattice factor Z_s, as expressed here, has been proposed by Hosemann and Bagchi[23] for the case of ideal paracrystalline statistics. Its derivation is based on the assumption that there is no coupling between the vector statistics defining the different edges of a cell in the paracrystalline lattice. This assumption may or may not have physical merits, but it does allow for a simplified mathematical expression in which the number of coordination statistics is reduced from 13 to 3. The use of this form of Z_s in the range of small q must be avoided, because the expression is ill-behaved in this region:

$$\lim_{q\to 0} Z_s(\mathbf{q}) = \prod_{k=1}^{3} [\delta_s/(\langle A_k \rangle \cos\alpha_k)]^2 + P(\mathbf{q} - \mathbf{0})$$

where α_k is the angle subtended by $\mathbf{q}$ and $\langle \mathbf{A}_k \rangle$ and P is the three-dimensional point function. The first term exhibits a singularity for $q \to 0$ if the direction of approach is such that $\alpha_k = \pi/2$ for any k. Also the value of the limit depends on the three α_k and is therefore not single valued. In order to minimize this computation problem in the present study, comparisons between model and experiment were limited to the q range above 0.25 nm^{-1}. As shown in Figure 5, the range studied included the SAXS interference maxima.

A single paracrystal exhibits anisotropic scattering; it is the random orientation of the macroscopic ensemble which gives rise to the observed isotropic scattering. Thus, if the number of paracrystals is large, the observer at a given q (i.e., given scattering angle) sees scattering for all $\mathbf{q}$ in the set $|\mathbf{q}| = q$. To facilitate this q-averaging process mathematically, it is necessary to evaluate the expression

$$(1/4\pi q^2)\int I_s(\mathbf{q})\, ds_q$$

where the integral is carried out on the surface of a sphere of radius q. $I_s(\mathbf{q})$ is the anisotropic scattering from a single paracrystal. The area integration was carried out using a straightforward Monte Carlo integration strategy.

To test the applicability of the model and to evaluate certain pertinent morphological parameters, the model described above was fit to each of the four SAXS powder patterns by using a nonlinear, least-squares, regression algorithm based on the method of steepest descent. The model has 6 degrees of freedom but was constrained to 5 by requiring that the crystalline volume fraction be as reported in Table II. In all cases convergence was observed, cross-correlation coefficients between parameters were sufficiently different from 1 or −1, and confidence intervals at 2 standard deviations were within 10% of the reported numbers.

These results are reported in Table III. Ellipsoid dimensions $\langle l_3 \rangle$ and $\langle l_1 \rangle$ are the average dimensions parallel and perpendicular to the axis of symmetry. In particular, the larger lateral dimensions match closely with the average dimensions in the [100] and [010] directions calcu-

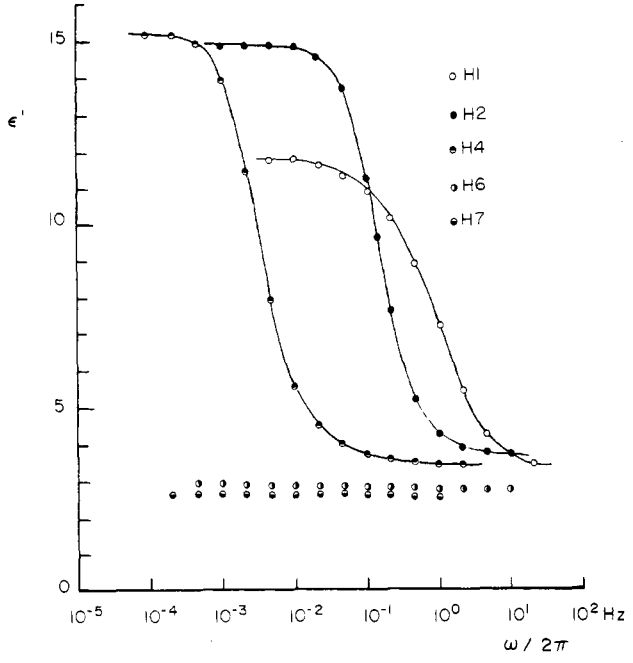

Figure 6. Dielectric permittivity spectra. Curves are best fits of dilute dispersion interfacial polarization model.[33]

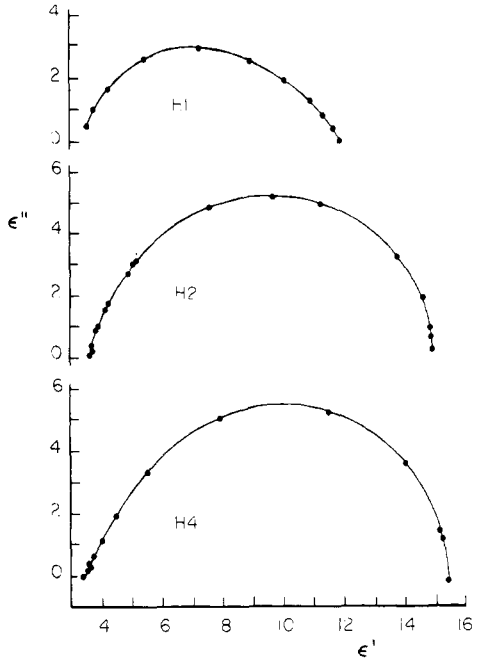

Figure 7. Argand diagrams of complex dielectric permittivity.

lated from diffraction line broadening reported in Table II. In all cases the ellipsoids are very oblate, so that the predictions are congruous with the expectation of crystalline lamellae. In the axial direction there is a slight trend among H2, H3, and H4 for lamellar thickening with increasing polyester segment degree of polymerization, although the H1 results are not in line. The model predictions for ξ, as predicted, show a tendency for decreasing electron density contrast with increasing overall polyester fraction u_2. In fact, as seen in Table III, the model predictions agree very well on this point with calculations based on phase densities and compositions. The lattice vector magnitudes, which are related to the average end-to-end lengths of the amorphous sequences, do not change much from polymer to polymer nor do the scalar fluctuation widths which are a measure of long-range disorder. The exception is again H1 which shows considerably larger disorder than do the other three polymers.

Subaudio Dielectric Spectroscopy. Spectra of the real component ϵ' of the complex permittivity are shown for H1, H2, H4, H6, and H7 in Figure 6. The ϵ' values are stated relative to ϵ_0, the permittivity of free space, 8.854 pF/m. Of these only H1, H2, and H4 show distinctive polarizations in the frequency range studied; the trend for this process to shift to lower frequency with increasing polyester fraction might explain its absence in the cases of H6 and H7. Whereas the measured data are shown as discrete points, the curves through the data are model fits as described below. In Figure 7 the dielectric loss factor ϵ'' is shown as a function of ϵ' for H1, H2, and H4. The departure from semicircular shape indicates that the process has a distribution of relaxation times.

Low-frequency polarizations in segmented polyether–esters have been studied by North et al.[27] and by Lilaonitkul and Cooper.[28] Both groups attributed the process to the polarization of free space charge in a multiphase medium, where one or more phases exhibits significant steady-state electrical conductivity. Due to an early reference to the process by J. C. Maxwell (1892) and elaboration by K. W. Wagner (1914), the process has become known as the Maxwell–Wagner loss process. These same processes are also referred to as interfacial polarizations; although it should not be inferred from this nomenclature that the charged particles are restricted to motion in a narrow interfacial region.

Proceeding along lines already established in modeling SAXS, the crystalline phase is approximated as an ensemble of ellipsoids, each with one axis of symmetry corresponding approximately to the [001] crystalline lattice direction. To reduce the number of model degrees of freedom, the dielectric permittivity of the crystallites is approximated as isotropic. Because these materials were formed under hydrostatic pressure, the ensemble orientation is random. The amorphous phase is modeled as an isotropic matrix. The intrinsic properties of phases are assumed fixed in the frequency range of observation.

The level of electrical conductivity in amorphous, rubbery polymers, particularly in the case of ionic conductivity, depends on the rate of micro-Brownian motion of the amorphous chains.[29,30] Such motion would be hampered in the case of amorphous chains immediately adjacent and covalently bonded to the (001) faces of the polyester crystallites. A reasonable model, therefore, contains an amorphous transition zone whose dielectric permittivity matches that of the amorphous bulk but whose electrical conductivity is somewhat reduced. This is facilitated mathematically by including a third phase with a confocal geometry separating the crystalline and bulk amorphous domains.

The model has been developed assuming a dilute dispersion of the included phase; ellipsoid–ellipsoid interactions are not included. This assumption has been made to reduce the number of model degrees of freedom, hopefully without loss of applicability. The crystalline phase in H4 has volume fraction 0.330, while these fractions are less in H1 and H2. Such a model has been developed by Stepin[31] and applied with some success to dilute aqueous suspensions:[32,33]

$$\hat{\epsilon} - \hat{\epsilon}_1 = (v_2/3)\ \mathrm{Tr}\ [\mathrm{M}]_{3\times 3} \qquad (11)$$

where $\hat{\epsilon}$ is the volume-average complex permittivity ($\epsilon' - i\epsilon''$), $\hat{\epsilon}_i = \epsilon_i - i\sigma_i/(\omega\epsilon_0)$, ϵ_i is the constant dielectric permittivity of phase i, where phase 2 is the dispersion of ellipsoids, phase 3 is the confocal shells, and phase 1 is the matrix, σ_i is the constant electrical conductivity of phase

Table IV
Subaudio Dielectric Spectroscopy

polymer	ϵ_1[a]	r_3/r_1[b]	σ_1/ϵ_0,[c] s^{-1}	σ_3/ϵ_0,[d] s^{-1}	$(1-\phi)/\phi$[e]
H1	3.79	0.068	33.1	1.05	0.447
H2	4.04	0.084	4.47	1.02	0.482
H4	4.06	0.103	0.0908	0.0141	0.488

[a] ϵ_1 is the permittivity of the bulk amorphous phase. [b] r_3/r_1 is the ratio of major axes lengths for a dispersion particle, where $2r_3$ is the length along the axis of symmetry. [c] σ_1 is the conductivity of the bulk amorphous phase. [d] σ_3 is the conductivity of the amorphous transition zone. [e] $(1-\phi)/\phi$ is the volume of the transition zone as a fraction of the volume of the crystallite. ϵ_0 is the permittivity of vacuum, 8.854 pF/m.

i, ω is the radial frequency of excitation, and Tr indicates the trace of the matrix, whose members m_{ij} are given by

$$m_{ii} = \hat{\epsilon}_1(\hat{\zeta}_i - \hat{\epsilon}_1)/[\hat{\epsilon}_1 + (\hat{\zeta}_i - \hat{\epsilon}_i)A_i]$$

$$m_{ij} = 0 \qquad (i \neq j)$$

$$\hat{\zeta}_i/\hat{\epsilon}_3 = [\hat{\epsilon}_3 + (\hat{\epsilon}_2 - \hat{\epsilon}_3)A_i + \phi(\hat{\epsilon}_2 - \hat{\epsilon}_3) \times (1 - B_i)]/[\hat{\epsilon}_3 + (\hat{\epsilon}_2 - \hat{\epsilon}_3)A_i - \phi(\hat{\epsilon}_2 - \hat{\epsilon}_3)B_i]$$

$$\phi = r_1r_2r_3/R_1R_2R_3$$

$$A_i = (r_1r_2r_3/2)\int_0^\infty ds/[(s + r_i^2)^2(s + r_1^2)(s + r_2^2)(s + r_3^2)]^{1/2}$$

$$B_i = (R_1R_2R_3/2)\int_0^\infty ds/[(s + R_i^2)^2(s + R_1^2)(s + R_2^2) \times (s + R_3^2)]^{1/2}$$

$2r_i$ is the length of the ith major axis of the ellipsoid, where $2r_3$ is along the axis of symmetry and $r_1 = r_2$, and $2R_i$ are the major axis lengths of the outer surface of the confocal shell. In the present case, where the ellipsoids and the confocal shells have axial symmetry about one axis, the integrals for the depolarization factors, A_i and B_i, can be evaluated analytically:

$$A_3 = \frac{1}{1 - (r_3/r_1)^2} - \frac{(r_3/r_1)}{[1 - (r_3/r_1)^2]^{3/2}} \arccos(r_3/r_1) \qquad [(r_3/r_1) < 1]$$

$$A_1 = A_2 = (1/2)(1 - A_3)$$

B_1, B_2, and B_3 are evaluated by replacing r_i by R_i. Because of the lack of ionic mobility in the immobilized crystalline phase, σ_2 is expected to be several orders of magnitude lower than σ_3 and can therefore be taken as zero. The crystalline phase permittivity ϵ_2 can be approximated by the permittivity of H7, 2.75.

If the matrix and shell phases have the same permittivity, $\epsilon_1 = \epsilon_3$, then, from eq 11, the high-frequency limit of ϵ' depends only on ϵ_1, ϵ_2, v_2, and the A_i's. The crystalline volume fraction is known from Table II and in the present case the A_i's depend only on r_3/r_1. Similarly, the low-frequency limit of ϵ' depends on the same quantities. The high- and low-frequency limits of ϵ' are available from the Argand diagrams in Figure 7. Since the phase 2 permittivity ϵ_2 and volume fraction v_2 are known, these two ϵ' limits can be used to determine ϵ_1 and r_3/r_1. The permittivity of the amorphous phase ϵ_1 is expected to change from polymer to polymer, as the composition of that phase changes. Values for ϵ_1 and r_3/r_1 are listed in Table IV for H1, H2, and H4. The trend for ϵ_1 to increase with increasing polyester fraction u_2 is expected, because the concentration of the more polar PTMT in the amorphous phase increases with u_2. The values for r_3/r_1 suggest that the ellipsoids are highly oblate; i.e., the crystals are lamellae. Although this result agrees qualitatively with that from SAXS modeling, comparisons between $\langle l_3\rangle/\langle l_1\rangle$ and r_3/r_1 show them to be quite different. The model formulation assumes that $\hat{\epsilon}$ depends on the shape of the dispersed particles but not on their size. Therefore, no size information is gained from a comparison of the dielectric spectra with the dilute dispersion model.

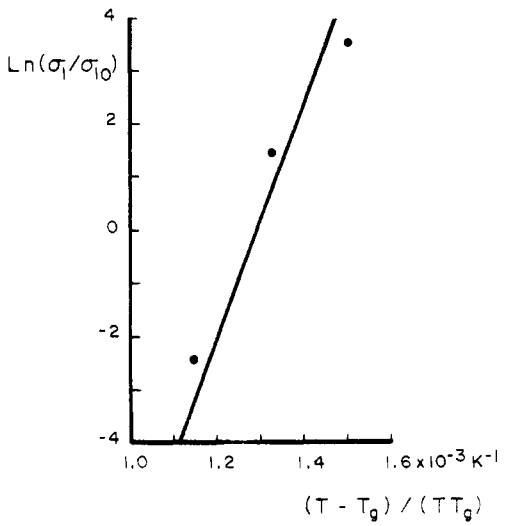

Figure 8. Arrhenius plot for bulk amorphous-phase conductivity. Apparent activation energy of curve fit from ref 28. σ_{10} is an arbitrary constant, 8.854 T Ω^{-1} m^{-1}.

The model dependence of $\hat{\epsilon}$ on the radial frequency of excitation ω is determined by the values of ϕ, σ_1, and σ_3. In order to evaluate these three parameters, nonlinear least-squares regression analysis was done for the ϵ' spectra. The analysis could have been done for the ϵ'' spectra as well. The two are not independent; the Kronig–Kramers relations allow for the calculation of one quantity if the other is known over the entire range where $\hat{\epsilon}$ exhibits frequency dependence. Therefore no new information can be gained from a similar analysis of the ϵ'' spectra. As seen in Figure 6, agreement between the data and the three-parameter regression fits was excellent over the entire frequency range studied. As with the SAXS analysis, correlation between parameters was acceptably low and the analysis returned high confidence in the resultant values. These values for ϕ, σ_1, and σ_3 are listed in Table IV.

The values for σ_3 are significantly lower than those for σ_1 in each of the three model fits, as expected. The transition-zone volume, as determined by this analysis, seems to be a constant fraction of the crystalline volume among these three polymers. The values of σ_1 decrease with increasing polyester concentration in the amorphous phase. Assuming that all polymers in the series have the same low amorphous-phase conductivity σ_{1g} at their respective glass transition temperatures T_g and the same apparent activation energy E_a for the process, their amorphous phase conductivities can be compared using

$$\sigma_1/\sigma_{1g} = \exp[(E_a/R)(T - T_g)/(TT_g)] \qquad (12)$$

where T is the test temperature (297 K). The temperature dependence for electrical conductivity, particularly ionic conductivity, in an amorphous polymer typically follows the WLF relation.[34] However, over a small range of temperatures an apparent activation energy can be calculated,

as has been done by Lilaonitkul and Cooper[28] using the audio frequency dielectric loss factor maximum corresponding to the primary transition. For H1, H2, and H4, E_a was calculated as 154, 182, and 216 kJ/mol, respectively. The average of these, 184 kJ/mol, has been used with eq 12 to draw the line in Figure 8, while the three data were taken from Table IV with T_g values approximated by the glass transition inflections on 10 K/min DSC traces. This analysis, although largely qualitative, does demonstrate the relation between σ_1 and T_g.

Discussion

Multiple, overlapped endothermic maxima are observed in the DSC traces for all polymers in this study. The DSC scan rate determines the relative sizes of the low-temperature and primary endothermic maxima; at low rates reorganization into thicker crystallites can occur during the scan, causing the size of the low-temperature melting endotherm to decrease and that of the primary endotherm to increase proportionately. The high-temperature endothermic maxima in H1 through H5 can also be explained by reorganization of the crystalline mass during the DSC scan. Due to this reorganizational behavior crystallinity calculations based on the apparent heat of fusion may be somewhat in error. Crystallinity calculations based on the nondestructive X-ray diffraction technique do not suffer from this shortcoming, although uncertainties regarding the nature and effect of lattice distortions, appropriate treatment of the incoherent component, etc., tend to compromise the effectiveness of that technique. In the present case, good agreement regarding heats of fusion among the DSC scan rates used and agreement between DSC and diffraction techniques for the crystallinity calculations lead to the conclusion that the calculated crystalline mass fractions are quite reliable.

No diffraction evidence was found for the existence of PTMT β crystallites, which are typically seen only in oriented materials. Among the α crystalline diffraction lines, all exhibited broadening. Diffraction lines from lattice planes whose perpendiculars have large components in the [001] lattice direction (parallel to the PTMT backbone) were particularly diffuse, suggesting that the crystallites are very narrow in the [001] direction, perhaps on the order of a few nanometers. The SAXS analysis was in agreement, predicting that the crystals were lamellae, 2–3-nm thick on average for H1 through H4. No evidence has been provided here, but chain folding may play an important role in incorporating some longer sequences into the lamellae, as demonstrated by Seymour et al.,[4] using gel permeation chromatography with acid-degraded remnants of PTMO–PTMT block copolymers. When combined with the average PTMT segment contour lengths, 4.2 nm for H1 to 11.4 nm for H4, these lamellar thicknesses are compatible with Hoffman's region III cluster model[35] for crystallization of highly subcoiled melts, where two to three stems connected by tight folds form clusters which are separated from each other by nonadjacent reentries or translamellar bridges. These amorphous sequences could well be made up of PTMO sequences. DSC quenches, performed at rates similar to those encountered in molding, exhibited undercoolings of 45 K and more in the cases of H1 through H4 so that the crystallizations do occur in the region III temperature regime. The Gambler's Ruin treatment of the fold-surface density paradox by Guttman et al.[36] rigorously prescribes that the minimum, average cluster size is two to three tightly folded stems. Models such as the "random switchboard" model give rise to very high amorphous densities at the crystal–amorphous phase boundary, this being highly unfavorable in a thermodynamics context. It should be noted that Guttman's analysis assumes that the stems run nearly perpendicular to the lamellar surface. The postulation of crystalline microdomains with convex surfaces or lamellae in which the stems are acutely angled with respect to the lamellar surfaces eases the above restrictions on the nature of chain folding. Lilaonitkul and Cooper[28] have developed light-scattering evidence suggesting that the second of these postulates, that of angled stems, may indeed hold sway in the melt-cast PTMT–PTMO microstructures. The PTMT crystalline lattices were assumed free from disorders of the second kind in crystal size calculations from line broadening. If second-order diffraction lines had been apparent in the diffraction profiles, it would have been possible to separate broadening due to small size from that due to long-range lattice disorder. Since no such lines were detected, the calculated crystal sizes in the [100] and [010] directions must be viewed as lower limits. The good agreement between these calculations and those from modeling SAXS are reassuring on this point.

The difference in electron density between the crystalline and amorphous phases was calculated by two methods. The first made use of measured densities and heats of fusion along with the calculated mass density for the crystalline phase and known stoichiometries. The second calculation was based on the fit of a kinematic scattering model to absolute SAXS intensities. Fair agreement between these two sets of values reflected positively both on the applicability of the SAXS model and on the assumption of a high degree of long-range order in the PTMT crystalline lattice.

In developing a SAXS model, the single PTMT crystallite was modeled as being enclosed by a spheroidal surface. This shape was chosen because of the analytical simplicity of its shape amplitude in reciprocal space. Comparisons between the shape amplitudes of spheroids and those of disks with similar volumes and aspect ratios showed only minor differences so that either could have been used in the analysis. Optical birefringence was reflected by the inclusion in the model of micron-scale superstructures in which the involved crystallites were assumed to be set in similar orientations. The scattering intensity that is calculated by eq 10 treats each superstructure as an independent scattering source. Transsuperstructure scattering was assumed to occur primarily at scattering angles lower than those modeled.

Comparisons of the scattering data with calculations based on a one-dimensional paracrystalline model showed that the two could not be matched in the region of the first-order scattering maxima. The model used allowed for both finite lateral extent and random ensemble orientation of the lamellar stacks.[37] The predicted scattering maxima was either too narrow or too low, relative to the diffuse background, depending on the choice of parameters. This result is contrary to the findings of Bandara and Droscher,[11] who found good correlation between a one-dimensional paracrystalline model with infinite lateral extent and the one-dimensional Fourier transform of the Lorentz-corrected isotropic scattering pattern. One problem with their approach is related to the tendency of the Lorentz correction, which is proportional to q^2, to deemphasize scattering at q values in the vicinity of the first-order scattering maxima. Also, the use of the Lorentz factor implies that the lamellar stacks have infinite lateral extent but provides no test of the assumption. The sharp, distinguishing features of $I(q)$ are not apparent in the Fourier transform of I, so that apparently good fits in the transform space do not guarantee a good fit of the model

to $I(q)$. Bandara and Droscher found crystal thicknesses of 3.5 and 3.3 nm for their materials A and B using calorimetry and SAXS data. On the basis of dilatometry and calorimetry, the same two thicknesses were calculated as 0.8 and 2.2 nm. The materials were quite similar to H2 and H3 of this study; the three-dimensional analysis used here yielded average crystalline thicknesses in the [001] direction of 2.3 and 2.8 nm. Bandara and Droscher calculated long spacings of 12.0 and 13.4 nm for polymers A and B, while the present analysis found average [001] lattice spacings of 12.0 and 11.3 nm for H2 and H3.

Bandara and Droscher[11] also predict the presence of a 0.9-nm-thick transition zone in which the electron density gradually changes from that of the crystalline phase to that of the bulk amorphous phase. The transition zone thickness calculations were done independently of the one-dimensional paracrystal modeling. This approach may lead to erroneous conclusions from one or both calculations; more correctly the two calculations should be combined. In the present study, adequate fits to the scattering data were obtained without the postulation of a density gradient at the phase boundary.

The question of the degree of interconnectivity between the crystallites in H1 through H4 is not easily resolved. The maximum crystallite dimensions, related to the average dimensions by $(4/\pi)^2$, in the [100] and [010] directions of the superlattice are similar to the lattice spacings in those same dimensions, indicating that the individual crystallites on any (001) plane of the superlattice may be somewhat interconnected. This would certainly help in explaining why these polymers exhibit significant mechanical hysteresis even at moderate strain levels.

In their study of interfacial polarization, North et al.[27] studied block copolyether–esters in which the polyester sequences were formed from randomly copolymerized PTMT and its isomer poly(tetramethylene isophthalate). Rather than making measurements in the frequency domain, the current density transient following a step change in electric field was Fourier transformed to obtain $\hat{\epsilon}(\omega)$. The current measurements exhibited electrode polarizations, which were extrapolated back from their long-time trends and subtracted from the traces before transforming; this procedure cannot be justified on a theoretical basis and may lead to large inaccuracies. A mean-field model, similar to the dilute dispersion model used here but without the transition zone, was used in an unsuccessful attempt to predict the high- and low-frequency limits of ϵ'. All parameters were estimated from auxiliary measurements except for the aspect ratio r_3/r_1, which was used as a parameter of fit. On the basis of this observation, the authors suggested that the polarization was not due to the polarization of space charge but rather to the polarization of charge trapped in a diffuse interfacial zone between phases. Lilaonitkul and Cooper[28] studied polymers similar to those of the present study. Large electrode polarizations were evident at the lowest frequencies, possibly due to incomplete dessication or insufficient electrode contact. The high- and low-frequency limits of ϵ' were estimated from the data and compared to the same model as used by North et al.[27] Lilaonitkul and Cooper found that reasonable limiting values could be calculated if the more conductive, amorphous phase was modeled as the dispersed phase. This approach appears to violate the assumptions of the dilute dispersion model, because the diminutive phase was modeled as the matrix.

In the present study, both the limiting values and the frequency dependence of ϵ' have been studied. The necessity for including a transition zone only becomes obvious when comparing the ω dependence of the data to that of the model without such a zone. In that case, the predicted distribution of relaxation times is much narrower than that of the data. The interfacial polarization modeling analysis yielded predictions of crystallite aspect ratio that were different by a factor of 2 or more from those calculated by SAXS modeling. It may be that the apparent particle in the dielectric model is actually an ensemble of particles on a single (001) superlattice plane. However, the dilute dispersion model, by ignoring specific long-range interactions may lead to erroneous calculations of r_3/r_1, as would the model of the previous studies,[27,28] which attempts to include nonspecific reaction field effects. Because the nonconducting domains are highly oblate and oriented, charge carriers diffusing through the matrix phase may be forced to follow tortuous paths. Such percolation phenomena are not germane to the dilute dispersion description. It is possible that such a process could be modeled, if the interdomain location statistics were known.[38,39] The possibility of combining a multipoint probability function approach to the calculation of dielectric permittivity with a lattice statistics approach to X-ray scattering analysis is currently being investigated.

Conclusions

For the PTMO–PTMT block copolymers of this study, it is reasonable to assume a two-phase model of microstructure. The crystalline phase involves only the α form of PTMT and is relatively free of lattice disorder, random thermal vibrations excepted. The amorphous phase can be modeled as a well-mixed blend of PTMO and uncrystallized PTMT. On the basis of polarized-light microscopy and the polarized-light scattering results of previous studies, the melt-cast morphologies are known to develop impinging spherulitic texture. Chain folding with adjacent reentry cannot alone model the propagation process, because the crystallizable PTMT sequences have contour lengths that are, on average, only a few multiples of the crystal thickness. This is especially true for the elastomeric systems, H1–H4, where the average polyester sequence lengths are shortest.

The single crystallites are themselves quite small, averaging only 2–4 nm in the [001] direction and 6–10 nm in the transverse directions. Evidence for these dimensions was developed by X-ray scattering studies at small and wide angles. The crystallized mass fraction tended to increase with overall polyester fraction and average polyester sequence length, although in none of the systems investigated did more than half of the PTMT crystallize. A three-dimensional kinematic scattering model of strictly two-phase morphology was developed to describe SAXS from micron-scale regions within the spherulites. The model calculations compared favorably with measured isotropic scattering patterns. The morphological parameters that emerged from this study suggest that in H2–H4 the individual crystallites, which are oblate, may coalesce to form extended, jogged multicrystalline structures. The distances separating the crystals in the [001] direction did not change much from polymer to polymer. Evidence for an amorphous transition zone of decreased electrical conductivity relative to the amorphous bulk was found in the dielectric spectra of interfacial polarizations. Since segment mobility adjacent to the (001) face of the PTMT crystallites is lower, this seems a reasonable conclusion. The nature of electrical conductivity in the amorphous phase is not certain. The lack of electrode polarizations at low frequencies suggests that electronic conduction predominates. However, the dependence of conductivity on $T - T_g$ is similar to that of diffusion processes in that

it obeys, to an approximation, the WLF rate–temperature equation. This dependence has often been observed for ionic conduction.

Registry No. (Dimethyl terephthalate)·(1,4-butanediol)·(poly(tetramethylene oxide)) (copolymer), 9078-71-1.

References and Notes

(1) E. J. Roche and E. L. Thomas, *Polymer*, **22**, 333 (1981).
(2) R. G. Vadimsky, *Meth. Exp. Phys.*, **16**, 185 (1980).
(3) G. K. Hoeschele and W. K. Witsiepe, *Angew. Makromol. Chem.*, **29/30**, 267 (1973).
(4) R. W. Seymour, J. R. Overton, and L. S. Corley, *Macromolecules*, **8**, 331 (1975).
(5) A. Lilaonitkul, J. C. West, and S. L. Cooper, *J. Macromol. Sci., Phys.*, **B12**, 563 (1976).
(6) L. Zhu and G. Wegner, *Makromol. Chem.*, **182**, 3625 (1981).
(7) J. W. C. van Bogart, D. A. Bluemke, and S. L. Cooper, *Polymer*, **22**, 1428 (1981).
(8) M. Gordon and J. S. Taylor, *J. Appl. Chem.*, **2**, 493 (1952).
(9) M. Matsuo, K. Geshi, A. Moriyama, and C. Sawatari, *Macromolecules*, **15**, 193 (1982).
(10) L. Zhu, G. Wegner, and U. Bandara, *Makromol. Chem.*, **182**, 3639 (1981).
(11) U. Bandara and M. Droscher, *Colloid Polym. Sci.*, **261**, 26 (1983).
(12) L. E. Alexander, "X-Ray Diffraction Methods in Polymer Science", Wiley, New York, 1969, p 77.
(13) J. D. Lake, *Acta Crystallogr.*, **23**, 191 (1967).
(14) O. Kratky, I. Pilz, and P. J. Schmitz, *J. Colloid Interface Sci.*, **21**, 24 (1966).
(15) M. A. Vallance, D. C. Faith, III, and S. L. Cooper, *Rev. Sci. Instrum.*, **51**, 1338 (1980).
(16) M. A. Vallance and S. L. Cooper, In "Computer Applications in Applied Polymer Science", T. Provder, Ed., American Chemical Society, Washington, DC, 1982, ACS Symp. Ser. No. 197, p 277.
(17) P. J. Flory, *J. Chem. Phys.*, **17**, 223 (1949).
(18) J. Runt and I. R. Harrison, *Meth. of Exp. Phy.* **16**, 287 (1980).
(19) M. Gilbert and F. J. Hybart, *Polymer*, **13**, 327 (1972).
(20) J. D. Hoffman and J. J. Weeks, *J. Res. Natl. Bur. Stand., Sect. A*, **66**, 13 (1962).
(21) M. Yokouchi, Y. Sakakibara, Y. Chatani, J. Tadokoro, T. Tanaka, and K. Yoda, *Macromolecules*, **9**, 266 (1976).
(22) U. Alter and R. Bonart, *Colloid Polym. Sci.*, **254**, 348 (1976).
(23) R. Hosemann and S. N. Bagchi, "Direct Analysis of Diffraction by Matter", North-Holland, Amsterdam, 1962, p 216.
(24) J. Wang and I. R. Harrison, *Meth. Exp. Phys.*, **16**, 128 (1980).
(25) W. Ruland, *Acta Crystallogr.*, **14**, 1180 (1961).
(26) W. Ruland, *Acta Crystallogr.*, **23**, 302 (1967).
(27) A. M. North, R. A. Pethrick, and A. D. Wilson, *Polymer*, **19**, 923 (1978).
(28) A. Lilaonitkul and S. L. Cooper, *Macromolecules*, **12**, 1146 (1979).
(29) S. Saito, H. Sasabe, T. Nakajima, and K. Yada, *J. Polym. Sci., Part A-2*, **6**, 1297 (1968).
(30) H. Sasabe and S. Saito, *Polym. J. (Tokyo)*, **3**, 631 (1972).
(31) L. D. Stepin, *Sov. Phys.-Tech. Phys. (Engl. Transl.)*, **10**, 768 (1965).
(32) H. Pauly and H. P. Schwan, *Biophys. J.*, **6**, 621 (1966).
(33) K. Asami, T. Hanai, and N. Koizumi, *Jpn., J. Appl. Phys.*, **19**, 359 (1980).
(34) J. D. Ferry, "Viscoelastic Properties of Polymers", 3rd ed., Wiley, New York, 1980, p 264.
(35) J. D. Hoffman, *Polymer*, **24**, 3 (1983).
(36) C. M. Guttman, E. A. DiMarzio, and J. D. Hoffman, *Polymer*, **22**, 1466 (1981).
(37) M. A. Vallance, Preliminary Report, University of Wisconsin—Madison, 1982.
(38) W. F. Brown, Jr., *J. Chem. Phys.*, **23**, 1514 (1955).
(39) W. E. A. Davies, *J. Phys. D*, **4**, 318 (1971).

Diffraction by Aperiodic Polymer Chains: The Structure of Liquid Crystalline Copolyesters

John Blackwell,* Genaro A. Gutierrez, and Robin A. Chivers

Department of Macromolecular Science, Case Western Reserve University, Cleveland, Ohio 44106.

Received May 19, 1983

ABSTRACT: The X-ray diffraction data for stiff-chain liquid crystalline aromatic copolyesters have been interpreted by calculation of the scattering characteristics of random copolymer chains. The meridional region of fiber diagrams of copolymers of *p*-hydroxybenzoic acid (HBA), 2,6-dihydroxynaphthalene (DHN), and terephthalic acid (TPA) and copolymers of HBA and 2-hydroxy-6-naphthoic acid (HNA) contains maxima that are aperiodic and shift in their positions depending on the monomer ratio. We have shown that excellent agreement is obtained between the positions of these observed maxima and those predicted for an aperiodic array of points where each point represents a monomer in a random chain, separated from adjacent points by the appropriate monomer lengths. Extension of these calculations to atomic models for the copolymer chains shows that only small changes occur in the positions of the predicted maxima, but there is now reasonably good agreement between the observed and calculated intensities.

Introduction

Copolyesters of *p*-hydroxybenzoic acid (HBA) and similar components form liquid crystalline melts, and this property can be utilized, e.g., to form high-strength fibers and novel molded plastics. A large number of thermotropic copolyesters have been reported in the patent literature, and their structures and properties have been reviewed by Jin et al.[1] We are using X-ray diffraction to study the structure of two groups of wholly aromatic copolyesters: copolymers of HBA and 2-hydroxy-6-naphthoic acid (HNA) and copolymers of HBA, 2,6-dihydroxynaphthalene (DHN), and terephthalic acid (TPA).

Schematic of the X-ray diffraction patterns of melt-spun fibers of three monomer ratios for each copolymer system are shown in Figures 1 and 2. These patterns indicate a high degree of axial orientation. The presence of sharp equatorial reflections suggests some order to the lateral packing, but the diffuse equatorial scattering, especially for the HBA/DHN/TPA system, points to extensive lateral disorder. The most striking features of the X-ray data are that the meridional maxima are aperiodic and also vary in position with changes in the monomer ratio. Analytical methods yield little information about the monomer sequence distribution in the copolymers, but the X-ray data argue against extensive blockiness. Rather it appears that we are dealing with largely or completely random sequences. These wholly aromatic copolymers will adopt stiff extended-chain conformations, and this stiffness will probably be independent of the monomer sequence.

We have derived the diffraction characteristics of rigid aperiodic polymer chains and have shown that the data are compatible with completely random sequences. In this

0024-9297/84/2217-1219$01.50/0